Functionalized and Platinum-Decorated Multi-Layer Oxidized Graphene as a Proton, and Electron Conducting Separator in Solid Acid Fuel Cells

Mhamad Hamza Hatahet [1], Maximilian Wagner [1,*], Andrea Prager [1], Ulrike Helmstedt [1] and Bernd Abel [1,2]

1   Department Functional Surfaces, Leibniz Institute of Surface Engineering, D-04318 Leipzig, Germany;
    Hamza.Hatahet@iom-leipzig.de (M.H.H.); andrea.prager@iom-leipzig.de (A.P.);
    ulrike.helmstedt@iom-leipzig.de (U.H.); bernd.abel@iom-leipzig.de (B.A.)
2   Wilhelm-Ostwald-Institute for Physical and Theoretical Chemistry, University Leipzig,
    D-04103 Leipzig, Germany
*   Correspondence: maximilian.wagner@iom-leipzig.de

Abstract: In the present article, electrodes containing a composite of platinum on top of a plasma-oxidized multi-layer graphene film are investigated as model electrodes that combine an exceptional high platinum utilization with high electrode stability. Graphene is thereby acting as a separator between the phosphate-based electrolyte and the platinum catalyst. Electrochemical impedance measurements in humidified hydrogen at 240 °C show area-normalized electrode resistance of 0.06 $\Omega \cdot cm^{-2}$ for a platinum loading of $\sim$60 $\mu g_{Pt} \cdot cm^{-2}$, resulting in an outstanding mass normalized activity of almost 280 $S \cdot mg_{Pt}^{-1}$, exceeding even state-of-the-art electrodes. The presented platinum decorated graphene electrodes enable stable operation over 60 h with a non-optimized degradation rate of 0.15% h^{-1}, whereas electrodes with a similar design but without the graphene as separator are prone to a very fast degradation. The presented results propose an efficient way to stabilize solid acid fuel cell electrodes and provide valuable insights about the degradation processes which are essential for further electrode optimization.

Keywords: solid acid fuel cell; graphene; atomic layer deposition; thin platinum film; stability

1. Introduction

Solid acids are an alternative and interesting class of proton conducting electrolytes for fuel cell applications. After Haile [1–4] demonstrated the general concept employing CsH_2PO_4 (CDP) in solid acid-based fuel cells (SAFCs) they were further developed by a number of researchers [1,3,5–15] and appreciated for their intermediate operating temperature (230–260 °C) in comparison to polymer electrolyte membranes fuel cells (PEMFCs). Although, SAFCs feature a number of advantages the use of solid acids for fuel cell electrolytes poses at least two major obstacles for their large-scale commercialization. The first is attributed to the high loading of the expensive catalyst materials in the electrodes. Over the last 10 years, numerous studies have been devoted to increasing the activity and reduction of the precious platinum metal catalyst. In a promising approach, a percolating network of platinum particles as electrodes catalyst was coated directly on the ionic conductor (CsH_2PO_4) by employing low-temperature metal-organic chemical vapor deposition (MOCVD) technique [16,17] or atomic layer deposition [18], wherein the platinum network acts as both the electrochemical catalyst and the electronic conductor. However, for low platinum loadings, insufficient percolation leads to a drop in power output [16,18]. Consequently, a relatively high platinum loading (>1.5 $mg \cdot cm^{-2}$) was needed [16]. A better strategy to improve the electrode's performance and durability with minimal platinum was to replace the percolating network of platinum with a conductive support decorated with the platinum catalysts. Because of the high electrical and thermal conductivity low-cost carbon materials have been used widely as supports [19–22]. Carbon black is currently

the most widely used support material to boost platinum activity towards the oxygen reduction reaction (ORR). These developments, in which a carbon support is employed, do not solve the second major problem, namely, the degradation and a lack of long-term stability. During SAFCs operation the platinum catalysts operate under relatively harsh conditions at the cathode, such as low pH, phosphate-containing electrolyte, high oxygen concentration and high temperature. Local hotspots were reported to cause local phase transitions [23]. Unwanted processes such as agglomeration of platinum nanoparticles (NPs) [20] or phosphate-associated catalyst poisoning are known for high-temperature PEMFCs and might occur as well in SAFCs [24,25]. The low-performance stability, in general, is an ongoing issue for SAFCs. Several more stable nanostructured carbon materials such as graphene film [26], reduced graphene oxide [27], carbon nanotubes (CNT) [28], and carbon whisker [29] were suggested and intensively investigated as platinum NPs catalyst supports. Haile et al. first employed platinum supported on carbon (3D) in the electrodes for SAFC application. The area-normalized electrode resistance (ANR) under anode conditions of the electrode was reported to be 0.06 $\Omega \cdot cm^2$ with a mass-normalized activity (MNA) equal to 2.16 $S \cdot mg_{Pt}^{-1}$ [1,30]. The ANR is calculated as the diameter of the area normalized Nyquist plot's arc. Later, Thoi et al. reported a larger electrode impedance of 1.2 $\Omega \cdot cm^2$, with higher MNA values of 78 $S \cdot mg_{Pt}^{-1}$ by synthesized platinum nanoparticles, via impregnation with H_2PtCl_6, directly on CNTs (3D) as a conductive substrate for SAFC electrodes [28]. Tennyson et al. [27] reported 1.3 $mg \cdot cm^{-2}$ platinum loaded on different carbon allotropes such as CNTs, carbon black, and graphene flakes. They also reported that platinum-decorated boron-doped graphene-like flakes exhibit higher stability toward oxidation during the aggressive SAFCs operating conditions, in comparison to CNT and polyhedral graphitic platelets. These hybrid materials showed a promising way for reducing anode and cathode catalyst loading with the enhancement of the platinum performance on the different carbon allotropes supports.

To synthesize platinum/carbon, several wet-chemical [31,32], and gas-phase processes [33,34] have been extensively studied. However, most of these methods, despite their simplicity and inexpensiveness, involve complicated steps and produce a wide range of platinum NP size distributions with high platinum loading and low productivity rates, which demonstrate poor long-term durability. Compared to these methods, [35,36] atomic layer deposition can have many unique inherent merits for preparing platinum NPs on carbon supports [37–44]. It allows the vapors of the precursor to interact separately with the substrates which enables the surface reactions to proceed in a self-limiting manner. The self-limiting nature of the surface reaction in atomic layer deposition (ALD) enables the controlled deposition of ultra-small metal amounts on complex 3D morphologies during each growth cycle [45–48]. This results in a conformal and uniform metal film over large and complex substrates, with precise control on film thickness, and excellent repeatability.

In the present work, a platinum-decorated oxidized graphene hybrid electrode was developed as a model electrode to assess the effect of the protective graphene membrane, between the electrolyte (CDP) and the electrocatalyst (platinum), on the electrode stability. For that purpose, multilayer (∼5-layers) graphene samples were oxidized with an atmospheric oxygen plasma. Platinum on a two-dimensional oxidized multilayer graphene is then deposited via ALD technology, creating a high surface thin-film platinum with adjustable thickness. The electrocatalytic activity was investigated via impedance spectroscopy with performance stability observed over 60 h in a constant voltage measurement.

2. Results and Discussion

2.1. Platinum-Decorated Oxidized Graphene

After transferring monolayer CVD-graphene film from the copper to silicon substrates, nearly continuous coverage with few holes and cracks can be seen in Figure 1a. The defects are mostly related to the etching process and the mechanical handling of graphene during transfer. In addition, SEM image indicates line defects such as grain boundaries and wrinkles. The grain boundaries are produced depending on substrates and processing

conditions, dividing the graphene film into many grains with different crystallographic orientations [49,50]. The wrinkles are formed during the cooling step in the growth of graphene due to different thermal expansion coefficients between the substrate (the copper foil) and the graphene [51]. Besides that, the SEM image highlights small few-layer graphitic islands on the continuous graphene film, as shown in Figure 1a. Multilayer (~5 layers) graphene films were synthesized via CVD (Figure 1b) and they were stable enough for use without risk of destruction during the treatment and transfer processes.
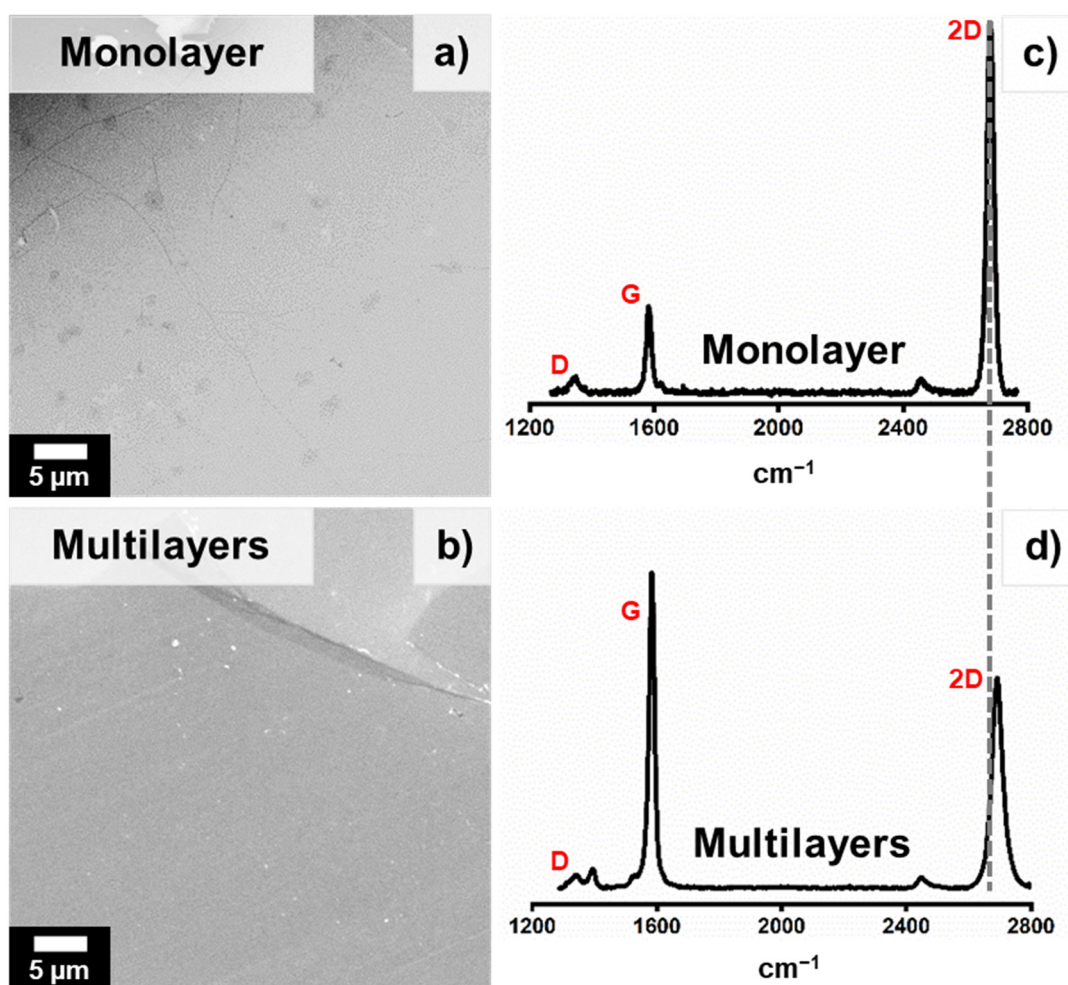

Figure 1. SEM images of transferred graphene films on silicon wafer: (**a**) Monolayer graphene film grown at working pressure equal to (1.3 Torr) throughout the graphene growth-step, (**b**) multilayers (~5 layers) graphene film grown at working pressure equal to (15 Torr) throughout the graphene growth-step. (**c**) The corresponding Raman spectra of transferred monolayer graphene on a silicon wafer and (**d**) is the corresponding Raman spectra of transferred multilayers (~5 layers) graphene on a silicon wafer. All graphene samples were transferred on a silicon wafer using PMMA and ammonium persulfate as an etchant.

The growth of monolayer, bi-layers, and triple-layers graphene using a CVD method and copper substrate was reported [52]. Changing the working pressure and H_2/CH_4 ratio allows controlling the number of graphene layers grown on copper by the thermal CVD [52,53], as shown in Figure 1. The Raman spectrum of different graphene-thicknesses films reveal three characteristic peaks at ca. 1348, 1590 and 2680 cm^{-1}, which are due to the D, G and 2D (G') bands respectively [54]. It is seen that the intensity ratio of G and 2D modes increases with the number of graphene layers [53]. A strong increase in the G band can be observed with increasing layer numbers changing the G to 2D ratio from 0.23 (Figure 1c) to 1.48 (Figure 1d). A blue-shift of the 2D peak position from

2680 cm^{-1} in single-layer graphene (Figure 1c) to 2695 cm^{-1} in the ~5-layers graphene (5L-Gr) occurred (Figure 1d) as well as an increase in the 2D FWHM (Full width at half maximum) from 28 cm^{-1} (monolayer graphene) to 58 cm^{-1} (5L-Gr), which be associated with the increase in the graphene layers [53,55]. Atomic force microscopy (AFM) was employed to measure the graphene nanosheet's thickness. The average thickness of the monolayer and 5L-Gr samples are determined to be about 0.35 and 1.6 nm, respectively. Based on a series of experiments, the 5L-Gr sample turned out to be optimal in terms of stability, resistance against oxidation and destruction and electron and proton conductivity for SAFCs application.

Problems when depositing platinum on graphene and other carbon allotropes are reported in the literature [56–58]. Due to the lack of interaction of platinum-precursor with the carbon surface, one popular strategy to facilitate deposition is to introduce oxygen functional groups (OFGs). In this work, tuning of OFGs on the multilayer graphene surface was achieved by atmospheric oxygen plasma treatment.

During plasma treatment, the oxygen-ion energy is transferred to the graphene when the oxygen-ion hits the carbon atom in the graphene lattice. This energy transfer leads to either rearrangement of the carbon ring and formation of Stone-Wales defects or remove the carbon atom from the lattice and creates vacancies [59], leading to the destruction of the graphene lattice [60]. A high-power plasma (100 W) with a short exposure time (8 s) was used for the 5L-Gr oxidation. Without completely destroying the 5L-Gr structure, these plasma processing conditions allow creating surface pits along the graphene samples with a sharp increase in the OFGs, which facilitate a highly homogeneous platinum distribution. Sample nomenclature hereafter follows the system OGr$_{X/Y}$, where "OGr" is oxidized graphene, "X" is the exposure time to plasma in seconds, and "Y" is the power of the used plasma in watt.

Turning to the graphene decoration with platinum films, the deposition of a uniform and continuous platinum catalyst on the oxidized graphene electrodes was achieved by atomic layer deposition (ALD). Trimethyl(methylcyclopentadienyl)platinum (IV) was used as a platinum precursor and oxygen as a co-reactant [61]. Sample nomenclature hereafter follows the system Pt$_{\textbf{ALD-X}}$ where X is the ALD cycles number.

The deposition of the platinum depends on the surface functionality of the multilayer graphene top surface. Figure 2a shows an SEM image of a freshly prepared 5L-Gr film on a copper substrate where the copper grains are clearly visible [62]. In the case of the untreated 5L-Gr film, platinum deposition occurs preferably on the edge, fold areas and grain boundaries, which are usually rich with defects and oxygen functional groups. Only a small fraction of platinum is deposited on the 5L-Gr basal plane due to its inertness and hydrophobic nature [63], as shown in Figure 2b. On the contrary, the ~5-layers oxidized graphene (5L-OGr$_{8/100}$) film exhibits very homogenous platinum deposition due to the high density of oxygen functional groups along the whole graphene surface, Figure 2c.

The evolution of the Pt$_{\textbf{ALD}}$ NPs on the 5L-OGr$_{8/100}$ surface depending on the number of ALD-cycles is shown in Figure 3. The SEM images after 150, 200, and 300 ALD cycles suggest that the platinum film nucleates on the OGr$_{8/100}$ substrate as discrete nanoclusters during the early stage of the ALD process, as shown in Figure 3a. As the number of cycles increases, the diameter and thickness of the nanoclusters are increased (see Figure 3b) and the islands begin to coalesce with adjacent platinum islands to form corrugated and continuous thin-film with worm-like structure at 200 ALD-cycles. The platinum islands continue to grow laterally after 300 Pt$_{\textbf{ALD}}$ cycles and the channels between neighboring islands start filling to eventually form a perfectly coalesced platinum layer on the 5L-OGr$_{8/100}$ surface, as shown in Figure 3c.
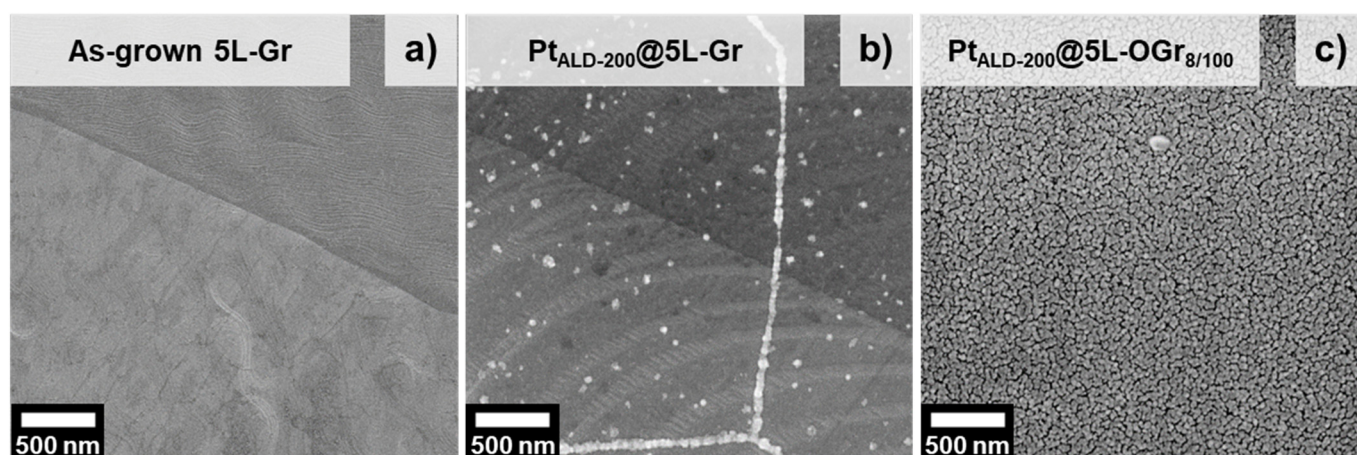
Figure 2. Representative SEM images of 5L-Gr on copper foils. (**a**) As-grown 5L-Gr without modification (**b**) Platinum decorated graphene after 200 ALD cycles (Pt$_{ALD-200}$@5L-Gr). (**c**) Oxygen plasma-treated graphene after 200 ALD cycles (Pt$_{ALD-200}$@5L-OGr$_{8/100}$).
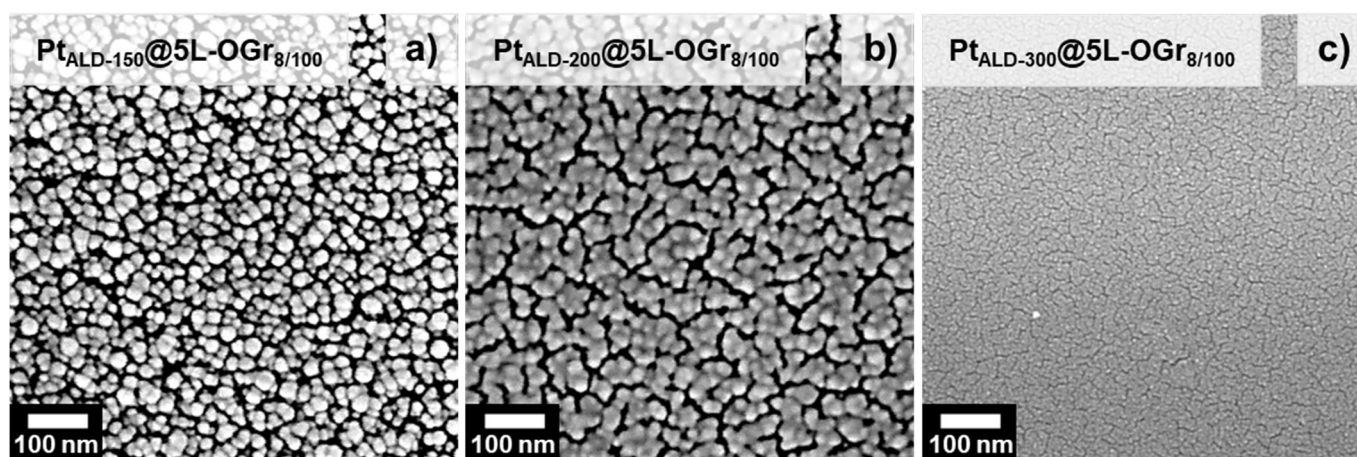

Figure 3. SEM images of 5L-OGr$_{8/100}$ samples after (**a**) 150 ALD cycles, (**b**) 200 ALD cycles, (**c**) 300 ALD cycles. All the platinum-decorated oxidized graphene samples are transferred onto a silicon wafer using PMMA and ammonium persulfate as an etchant.

2.2. Electrochemical Measurements and Performance

We investigated the electrode performance as a function of the platinum-film thickness. A series of samples were prepared by sputtering different thicknesses of platinum directly on the CsH$_2$PO$_4$ pellets as shown in Scheme 1b. The sputtered sample nomenclature hereafter follows the system Pt$_{SP-X}$, where X is the sputtered Pt-film thickness in nanometres.

The ANR measured under the same anode SAFCs conditions of different Pt-Sputtering electrodes are shown in Figure 4a. The Nyquist plots are shown in electronic supplementary Information Figure S1. Based on the ANR results, the maximum electrode activity was measured with Pt$_{SP-8}$ electrode, which suggests that the electrode performance is not limited by the catalyst content. The hydrogen oxidation reaction is taking place dominantly at the two-phase boundary between CsH$_2$PO$_4$ and platinum, with hydrogen diffusing through the platinum layer. Thick layer sizes are not increasing the active site density but hampering the hydrogen diffusion and decreasing triple-phase boundaries [2,4,27,64].
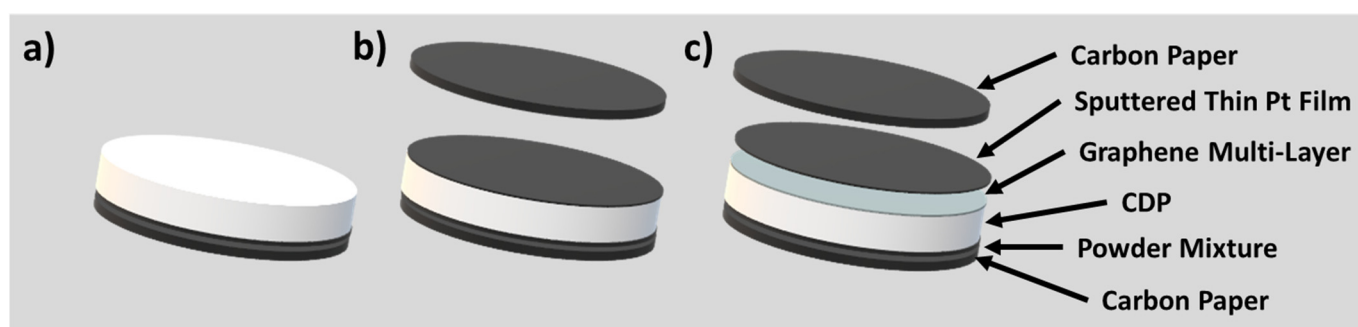
Scheme 1. A cartoon showing the Pt$_{SP}$ cell fabrication: before (**a**) and after (**b**) the sputtered thin Pt film and (**c**) the sputtered thin Pt film in the presence of graphene separator.
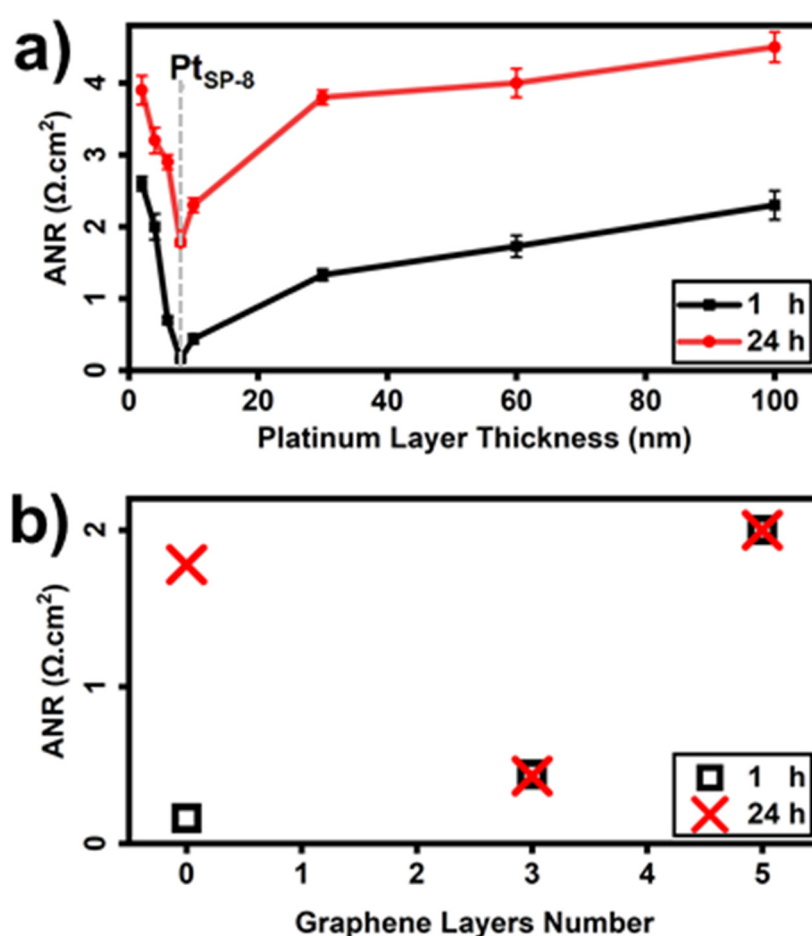

Figure 4. Measurements of the ANR were obtained by impedance spectroscopy under anode conditions. (**a**) Dependency of the ANR with the platinum film thickness of graphene-free electrodes. The platinum was deposited using magnetron sputtering. (**b**) Dependency of the ANR of Pt$_{SP-8}$ electrodes in the presence of graphene layers with varying thicknesses. The graphene was transferred to the CDP surface before platinum deposition via magnetron sputtering using PMMA and iron chloride in hydrochloric acid as an etchant.

The ANR tendency of different platinum layer thicknesses was in agreement with the work of Louie et al. [65]. They reported the lowest anode impedance for symmetrical cell measurements for a thickness of 7.5 nm. However, independent of the platinum layer thickness, the ANR increased significantly over the course of 24 h, Figure 4a. This could be changed by introducing a graphene separator between the CDP and platinum layers. Graphene attracted considerable interest because of its unique electrical, thermal, and me-

chanical properties [66–74]. These properties are affected by the graphene layers number, whereas the conductivity decreases with the increase in the graphene thickness [75–84]. The same trend was observed for Pt_{SP-8}@3L-Gr and Pt_{SP-8}@5L-Gr cells shown in Figure 4b. Samples were fabricated as shown in Scheme 1c with different graphene layers numbers and measured under the same anode SAFCs conditions. The ANR after one hour was lowest for the graphene-free cell, while the resistance increased considerably to 0.4 $\Omega \cdot cm^2$ for Pt_{SP-8}@3L-Gr and to 2 $\Omega \cdot cm^2$ for Pt_{SP-8}@5L-Gr. The corresponding Nyquist plots are shown in electronic supplementary Information Figure S2. The presence of the graphene separators affected the electrode stability and activity remarkably. The presented results indicate that the proton passes through the graphene material. While the electrons conductivity of multi-layers oxidizing graphene/graphene can be rationalized, it is important to note that the diffusion process of the protons through these materials is unclear and still subject of intense debate. Graphene is a good electrical conductor and therefore can improve the charge transfer behavior of the electrode. The proton motion through the Pt-graphene interface and graphene layers can be frequency-dependent and may contribute to the ANR. Several papers and reviews have appeared over the last ten years on this topic [85–91]. The through-plane proton conductivity of the multilayer graphene samples can be possibly ascribed to different factors: (i) Geim et al. reported that the proton transport can be further enhanced by decorating the graphene membranes with catalytic metal nanoparticles [89]. (ii) The through-graphene proton transport is strongly dependent on the relative humidity (RH) and temperature for the multi-layer graphene membrane. A higher RH [87] and temperature [89] tend to give higher proton conductivity. (iii) The presence of CsH_2PO_4 with water might assist the expansion of interlayer spacing [88] and increasing the water-absorbing capacity through the phosphate anion, which generates additional pathways for proton hopping [86,87]. Finally, (iiii) as mentioned above, the as-grown CVD graphene films contain defects, graphitic islands, and many polycrystalline grains with different crystallographic orientations stitched at the grain boundaries along the whole surface. The grain boundary in polycrystalline graphene sheet is a periodic arrangement of pentagon−heptagon pairs along the boundary which is a favorable site to adsorb extrinsic impurities (e.g., oxygen, hydroxyl, hydrogen, etc.) [92,93]. Increasing the content of the oxygen functional group enhances the proton hopping and thus increase the protonic conductivity [94].

　　Pt_{ALD}-decorated oxidized graphene cells were characterized using impedance spectroscopy under anode conditions as well as CstV measurements under fuel cell conditions. The charge transfer resistance measured under anode conditions for $Pt_{ALD-200}$@5L-OGr$_{8/100}$ (59 $\mu g_{Pt} \cdot cm^{-2} \pm 2$) and $Pt_{ALD-300}$@5L-OGr$_{8/100}$ (91 $\mu g_{Pt} \cdot cm^{-2} \pm 2.3$) electrodes are shown in Figure 5a,b, respectively. The electrode after 200 ALD cycles shows significantly lower resistance than the electrode prepared by 300 ALD cycles, despite the lower platinum loading. Based on the very low amount of platinum this results in a very high MNA of about 280 $S \cdot mg_{Pt}^{-1}$.

　　The performance of the $Pt_{ALD-200}$@5L-OGr$_{8/100}$ cathode exhibited relatively high stability, as observed in the constant voltage measurement at 0.35 V in Figure 5c, especially compared to the Pt_{SP-30} cathode (54 $\mu g_{Pt} \cdot cm^{-2} \pm 3$) that has a similar platinum thin-film design but no graphene separator between the electrolyte and the catalyst. During the first 1.5 h, the current density of the $Pt_{ALD-200}$@5L-OGr$_{8/100}$-MEA increases. We attribute the observed increasing current density to the removal of the PMMA-residues and/or to sintering of the electrolyte layer [64]. After the initial increase period, the current density of the electrode decreases by only 0.15% h^{-1}. A small jump can be observed after 23 h. This jump was reported previously by Lohmann et al. and it is due to slight changes of the electric connections and not inherent to the electrodes [64]. The platinum-decorated oxidized graphene electrodes show a higher activity compared to the graphene-free Pt_{SP-30}-MEA. One possible explanation for the higher performance is the interfacial design and the highly conformal Pt_{ALD} coatings of the platinum/oxidized graphene hybrid electrode, in particular the triple-phase boundary [27,64].
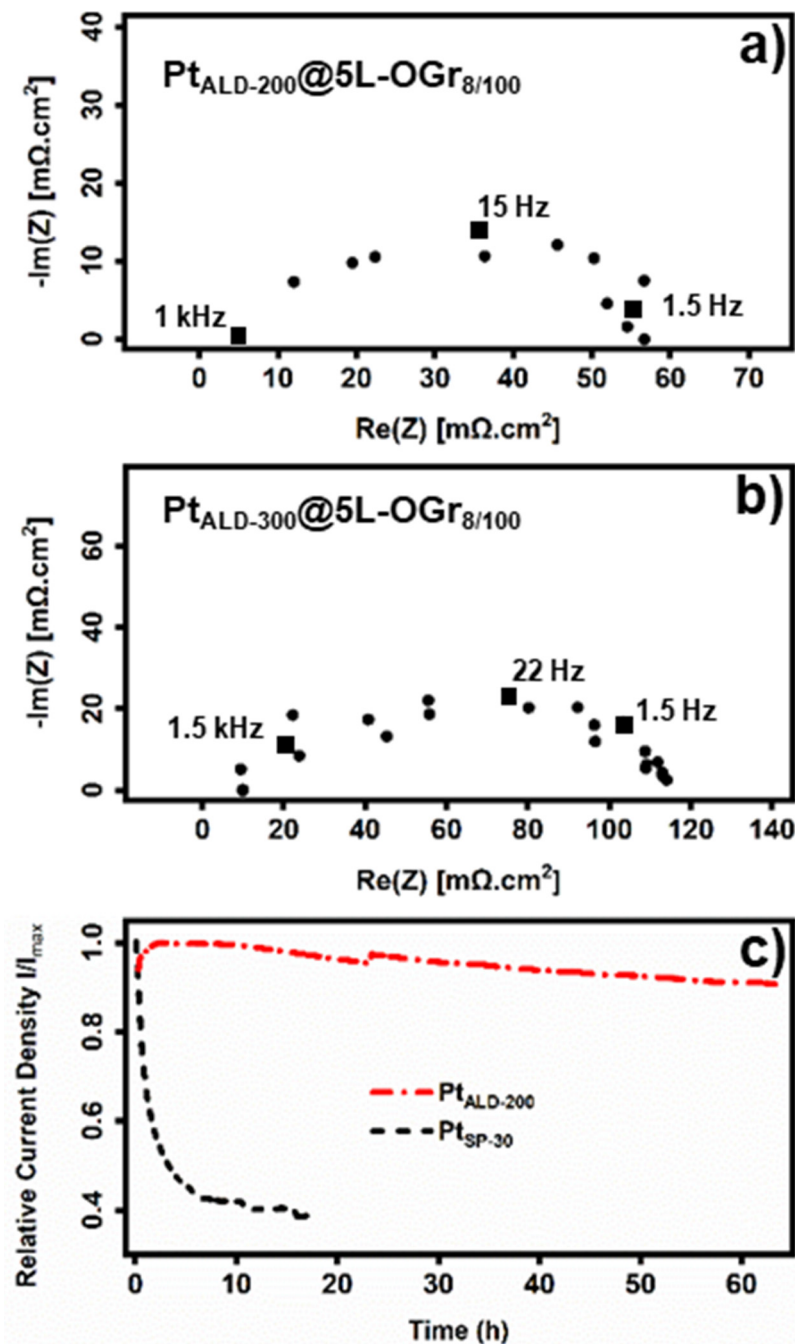
Figure 5. Nyquist Plot of the electrode impedance of the Pt$_{ALD}$@5L-OGr$_{8/100}$ samples measured under anode conditions after (**a**) 200 and (**b**) 300 ALD cycles. The electrolyte resistance was subtracted in both cases. (**c**) The current density of the Pt$_{ALD-200}$@5L-OGr$_{8/100}$ sample (dashed–dotted line) over 60 h was measured at 0.35V under fuel cell conditions. The electrodes based on 30 nm Pt films sputtered directly on the CsH$_2$PO$_4$ pellets are included for comparison (dashed line) in (**c**). All the platinum-decorated oxidized graphene samples were transferred using PMMA and iron chloride in hydrochloric acid as an etchant. The open-circuit voltage was 0.88 V for the Pt$_{ALD-200}$@5L-OGr$_{8/100}$ sample and 0.86 V for the Pt$_{SP-30}$ sample.

We assume that the nanopatterned structure of the Pt$_{ALD-200}$ film improves the SAFCs performance by enhancing the proton and electron pathways through two-dimensional hybrid electrode structure, resulting in the effective mass transfer of reactants and products and leading to an increase in the electrochemically active surface area and better platinum utilization at the electrode. Furthermore, the worm-like structure facilitates the fuel gases

replenishment and boosts the removal of the reaction products at the electrodes. The most interesting difference between the $Pt_{ALD-200}$@5L-OGr$_{8/100}$ and the graphene-free Pt_{SP-30}-MEA, however, is the significant improvement in stability Figure 5c. While the current density of the Pt_{SP-30}-MEA decrease rapidly by $\sim$60% within the first 10 h, the current density of the $Pt_{ALD-200}$@5L-OGr$_{8/100}$-MEA showed a degradation rate of 0.15% h^{-1}.

Wagner et al. reported a morphological change of CsH_2PO_4 around the current collectors [12,23] and associated them with the CDP phase transition triggered by local hot spots. Originating from these morphological changes different degradation mechanisms were suggested including a deterioration of the catalyst–current collector network and a slow poisoning of the platinum. Contamination of platinum by phosphate ions is well known once the platinum is in contact with free phosphate ions, as is the case for phosphoric acid-based fuel cells [24,25]. Graphene material seems to act as a stable separator between the electrolyte and the electrocatalyst, providing sufficient coverage of the electrolyte surface and preventing the platinum catalysts from being contaminated. The high current conductivity of the graphene layer can further stabilize the connection between the platinum layer and the current collector, preventing isolated areas.

3. Experimental, Materials and Methods

Unless otherwise specified, chemicals and reagents were used as received from the supplier without further purification.

3.1. Graphene Preparation via Chemical Vapor Deposition (CVD) on Copper Substrate

Single-layer graphene targets made with a rapid thermal processing cold wall reactor (Moorfield nanoCVD, Knutsford, Cheshire, UK), where the copper foil (Alfa Aesar, 99.999%, Kandel, Germany) is heated through a heating stage, and performed in a six-stage process: (I) as-received copper foil is heated to (930 °C) at a heating rate of 9 °C/s in an atmosphere of Ar (flow 198 standard cubic centimeters per min (SCCM)) and H_2 (flow 2 SCCM) gases under vacuum ($\sim$3 Torr). (II) The substrate is annealed for 2 min under the same condition as in stage (I) to reduce the oxides on the copper surface and for grain growth. (III) Follow by ramping in the temperature, of the heating stage, from 930 °C to 1030 °C for over 5 min, then, (IV) another annealing step for 30 min under the same atmosphere condition as in stage (I). For graphene growth (V), a mixture of Ar/CH_4/H_2; Ar pressure 1.04 Torr (flow 40 SCCM), H_2 pressure 0.21 Torr (flow 8 SCCM) and CH_4 pressure 0.05 Torr (flow 2 SCCM) gas is then used while the chamber pressure was maintained at 1.3 Torr for 30 min. Finally (VI) the graphene | copper foil is cooled to room temperature. Multi-layers graphene samples were grown on the copper substrate by increasing the working pressure during the growth step.

3.2. Graphene Transfer

Because of the fluorescence background of the copper foil during the RAMAN measurement, a transfer of graphene to a more suitable substrate (e.g., SiO_2) is required to determine the graphene quality. Additionally, transfer the graphene onto the arbitrary substrates is a critical step in the use of CVD-grown graphene for the most practical applications. In the lab, as-grown graphene films were transferred onto different substrates by wet chemically etching of the copper foils in aqueous solutions of ammonium persulfate (Sigma-Aldrich, $\geq$98.0%, Taufkirchen, Germany) or iron (III) chloride (VWR, 99–102%) in hydrochloric acid (HCl, Sigma-Aldrich, 37%, Taufkirchen, Germany). The use of oxidant-etchant solutions such as $FeCl_3$ causes significant contamination of the graphene surface with iron species [95]. The presence of iron-metallic impurities alters the efficiency and durability of the metal-decorated graphene electrode. These changes, however, gained less coverage in this article and will be discussed elsewhere in depth. Before the wet etching, the surface of graphene | copper was spin-coated with polymethyl methacrylate (PMMA, Sigma-Aldrich, Taufkirchen, Germany). PMMA was dissolved in chlorobenzene

(Alfa Aesar, 99.5%, Kandel, Germany) with a concentration of 0.05 mol dm^{-3} (4.6 g of PMMA–100 mL of chlorobenzene).

Raman spectroscopy reveals that graphene is grown on copper foil. Since ammonium persulfate/iron chloride solutions etch only copper, therefore, the bottom-side of the copper foil was floated on nitric acid (HNO$_3$, Merck KGaA, 65%, Darmstadt, Germany): milli-Q water (1:1.5 *v/v*) for 30 s to etch the bottom-side graphene and provide an appropriate profile for the etchant to copper. After the etching of the bottom graphene, the PMMA|graphene|copper film was sequentially cleaned in milli-Q water in three separate Petri dishes. Then, 100 mL of the ammonium persulfate (0.04 M) or iron chloride (0.22 M) in hydrochloric acid (1 M) was poured into a crystallizing dish where the PMMA|graphene|copper sample was allowed to float on the etchant's surface, carried by surface tension forces. A glass cylinder with open ends and a slightly smaller radius than the crystallizing dish was inserted into the dish, forming a double-walled cylinder, however, suspended in order to leave a small gap between the cylinder and the bottom of the dish [96]. After 8 h, the dissolution of the copper foil was complete and the etchant was removed with Q-milli water by repeatedly draining out the waste solution and adding in milli-Q water, through the inter-wall region between the crystallizing dish and the glass cylinder, until neutral pH was reached. This setup allows the exchange of the etchant by the millipore water without turbulent flow close to the graphene layer and hence avoids ripples and folding. Then, the graphene layer is transferred onto the desired substrates and dried with a gentle nitrogen stream. As a final step, the PMMA layer was dissolved by acetone and then the graphene was annealed for 12 h under a high vacuum ($\sim 7 \times 10^{-8}$ Torr) at 120 °C after the transfer process.

3.3. Oxygen Plasma Treatment

The CVD-graphene films on copper foils were exposed to gas plasma with a radio frequency (RF) plasma system (Junior Plasma System, Europlasma NV, Oudenaarde, Belgium) equipped with a 300-W kHz generator. In the treatment process, the vacuum chamber was pumped down to ~120 mTorr. When the base pressure was reached, 20 SCCM of oxygen gas was introduced into the chamber via a mass flow controller (MFC) during a stabilization phase of 180 s. After the stabilization of the pressure, the oxygen plasma was generated by the radio frequency (RF:13.56 MHz) power source. The samples were exposed to plasma for varying times at a working pressure of 180–195 mTorr with a radio frequency power of 100 W. During the time of plasma treatment, the temperature inside the chamber increased from 25 °C to 27 °C. After plasma treatment, all samples were stored in a nitrogen environment.

3.4. Catalyst Deposition
3.4.1. Atomic Layer Deposition (ALD)

Platinum deposition on oxidized graphene substrates was carried out using a home-built ALD instrument, which provides thermal enhanced ALD configuration. The samples were loaded on a stainless-steel sample holder, which was then transferred into the ALD reactor through a load-lock and placed in the center of the reactor. The temperature of the substrate heating plate in the chamber was maintained at 275 °C. The reactor was then evacuated and thermally equilibrated overnight.

Commercially available trimethyl (methylcyclopentadienyl) platinum (IV) (Pt(MeCp)Me$_3$, Strem Chemicals, 99%, Newburyport, MA, USA) was used as the platinum precursor and oxygen as the co-reactant. Because MeCpPtMe$_3$ is air-sensitive, it was loaded to a customized stainless-steel bubbler (Swagelok) in a glovebox and then connected directly to the system without exposition to air. The temperature of the solid precursor was maintained at 50 °C in the bubbler to provide enough vapor pressure. The Pt(MeCp)Me$_3$ vapor was carried by heated nitrogen into the ALD process chamber, through a delivery line which was heated to 130 °C. Ultrahigh purity Nitrogen (99.9995%) was used as a carrier gas at a flow rate of 150 SCCM. N$_2$ was also used to remove unreacted precursors and any

byproducts during the reaction. The oxygen was pulsed into the reactor through a needle valve and a solenoid valve with a flow rate of 60 SCCM during a continuous flow. A static exposure mode was applied during both ALD half-cycles. The pulse time of the Pt(MeCp)Me$_3$ precursor was 1 s, after which the valves to the pumping system were kept closed for another 10 s to prolong the dwell time of the precursor, resulting in a total exposure time of 11 s, followed by an N$_2$ gas purge for 80 s, in order to completely remove the reactant gases, then evacuation for 40 s, and then a pulse of O$_2$ dose for 1 s, followed by another N$_2$ gas purge for 80 s and evacuation for 40 s. Since our reactor is relatively large, the exposure time of the graphene samples to Pt(MeCp)Me$_3$ vapor was crucial for platinum deposition. Besides, this 10 s soaking step reduces the platinum precursor usage and enables a self-limited platinum growth on the oxidized graphene surface.

3.4.2. Sputtering

The platinum depositions on the substrates were achieved in the Edwards Auto 306 RF Magnetron Sputtering System and the film thickness was measured in real-time during deposition using a quartz crystal microbalance measurement.

3.5. Electrochemical Cell Characterization

3.5.1. Platinum-Decorated Oxidized Graphene Cell Fabrication

The synthesis of the CsH$_2$PO$_4$ was achieved by dissolving the starting reagents Cs$_2$CO$_3$ (Alfa Aesar, 99.99%) and H$_3$PO$_4$ (Carl Roth, ≥85%, Karlsruhe, Germany) in a molar ratio of 1:2 separately in methanol (Carl Roth, ≥99%). The two solutions were mixed and stirred for 1 h at 1500 r.p.m. Methanol was added to induce immediate precipitation of CsH$_2$PO$_4$ particles. The CsH$_2$PO$_4$ powder was then filtered, washed with additional methanol and dried at 80 °C. Finally, CsH$_2$PO$_4$ went through an additional lyophilization step (for 12 h) just before using to remove surface-adsorbed water and detract its influence on transport properties.

The platinum-decorated oxidized multi-layer graphene cells were structured in two steps. In the first step and for all graphene cells tested, identical anodes with a platinum loading of 7.7 mg·cm^{-2} were formed from the powder mixture as described by Uda and Haile [3]. Briefly, the powder-mixture electrode was prepared by mixing and grinding CsH$_2$PO$_4$, platinum-black (Sigma-Aldrich, 99.9%, fuel cell grade), platinum on carbon (Alfa Aesar, HiSPEC 4100), and naphthalene (Alfa Aesar, 99+%) in a 3:3:1:0.5 mass ratio. Then, the carbon paper discs (Toray TGP-H-120) and the CsH$_2$PO$_4$ membrane were pressed uniaxially in a hydraulic press (Atlas Auto 15T, Specac Ltd., London, UK) to the anode, maintaining 200 MPa for 20 min, as shown in Scheme 2a.
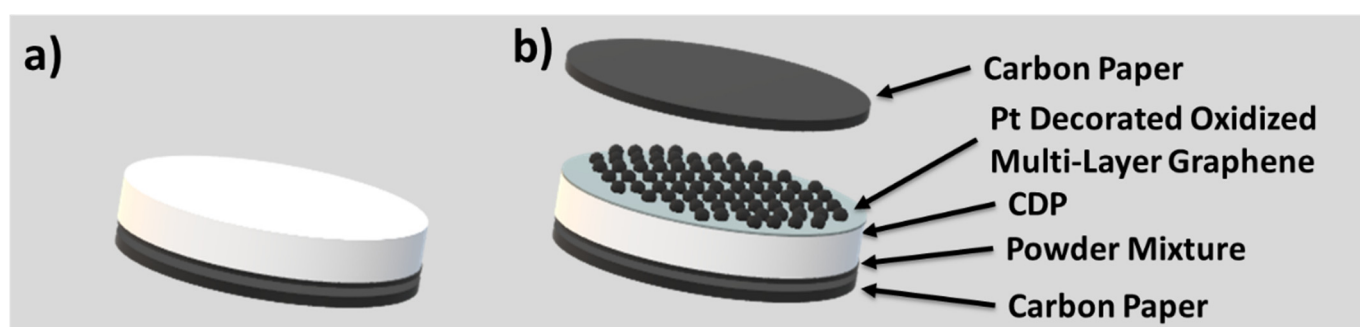
Scheme 2. A cartoon showing the platinum-decorated oxidized multi-layer graphene cell fabrication: (**a**) The first step and (**b**) the second step. For each membrane electrode assembly (MEA) a total of 160 mg·cm^{-2} (thickness = 0.6 mm) of the electrolyte powder was used.

The second step was started with the transfer of platinum-decorated oxidized multi-layer graphene (PDG) by wet chemical etching of the copper foils (as described in Section 3.2). The double-walled cylinder system was applied and iron chloride in hydrochloric acid was

used. However, an additional step after removing the etchant was added. Then, 250 mL of acetone (Merck, ≥99.8%) was poured gently into the water. This step was crucial to avoid damaging or dissolving the CsH_2PO_4 surface after transfer of the wet (PMMA | graphene or PMMA | PDG). The pellets Scheme 2b were then stored under vacuum (~6 Torr) for 48 h in order to improve the adhesion between the graphene and the CsH_2PO_4 surface. Finally, the PMMA layer was removed by pure acetone followed by a vacuum annealing step at 120 °C for 12 h directly before the impedance measurement.

3.5.2. Impedance Spectroscopy

The electron transfer kinetics of hydrogen electrooxidation in each electrode was studied by selected electrochemical impedance spectroscopy (EIS) measurements (Biologic, VSP300, Seyssinet-Pariset, France). The fuel cells were placed between stainless steel porous meshes (GKN Sinter Metals Filter GmbH, Radevormwald, Germany), which are served as gas diffusion layers. AC impedance measurements were performed over the frequency range 10 mHz to 7 MHz with an applied voltage amplitude of 10 mV. Data were collected at 240 °C, with the sample chamber maintained in a humidified H_2 atmosphere ($p(H_2O)$ = 0.4 atm) by flowing the inlet gases (flow 30 SCCM) through a Q-water bubbler (inhouse construction) held at 80 °C. During heating and cooling, Ar gas purge 120 SCCM was used to avoid the possibility of condensation on the cells. The constant voltage measurements were performed at 240 °C using 50 SCCM pure oxygen and hydrogen flow, each at a dew point of 80 °C.

3.6. Characterization Methods

Atomic force microscopy (Bruker Dimension Icon AFM, Billerica, MA, USA) using OTESPA-R3 cantilevers, in tapping mode, characterized the surface morphology of graphene samples on SiO_2/Si wafer. The obtained data were plane-corrected with the SPIP 6.7.3 software. Scanning electron microscope (SEM) imaging was performed with an Ultra 55 SEM (Carl Zeiss Microscopy GmbH, Jena, Germany) at 2 kV using the in-lens detector. Raman spectrum is recorded using a laser with a 532 nm excitation wavelength at a very low laser power level (to avoid any heating effect) coupled to a Horiba LabRam confocal (X100 Olympus MPlan objective, Center Valley, PA, USA) spectrometer with a resolution of 1.3 cm^{-1} (600 lines/mm grid to record both the 2D-peak and the G-peak simultaneously). The mass fraction of platinum on graphene samples was determined using inductively coupled plasma optical emission spectroscopy (ICP OES, SPECTRO Ciros Vision, SPECTRO Analytical Instruments GmbH, Kleve, Germany). The use of analytical techniques such as ICP OES provides more precise and accurate results regarding analyte concentration determination [97–99]. The platinum sample was digested in 28% *vol/vol* acid solution with a 6:1 volume ratio of HCl:HNO$_3$ in Millipore water for 30 min. Afterward, microwave (MLS Mikrowellen Laborsysteme, microPREP, Leutkirch, Germany) digestion was carried out for 40min heating at 235 °C followed by another digestion step for 24 h at RT.

4. Summary and Conclusions

The treatment of multilayer graphene (~5-layers) with atmospheric plasma results in a material that has a finite thickness, mechanical stability and features proton and electron conductivity. With these features, the oxidized multilayer graphene membrane is an ideal substrate and separator for the platinum catalyst and the electrolyte in the intermediate temperature fuel cell electrodes. These hybrid electrodes were designed in a way to be easily characterized but at the same time, the electrochemical impedance measurement in humidified hydrogen for the Pt$_{\text{ALD-200}}$@5L-OGr$_{8/100}$ electrode displays a relatively low ANR (0.06 $\Omega \cdot \text{cm}^{-2}$), with a very low platinum loading prepared by 200 ALD cycles (59 μg$_{\text{Pt}} \cdot \text{cm}^{-2}$ ± 2), resulting in a very high mass-normalized activity of about 280 S·mg$_{\text{Pt}}^{-1}$. Platinum-decorated cathodes utilizing oxidized multi-layers graphene operates with high stability over 60 h, while a similar cell without graphene was prone to rapid degradation.

This study demonstrates promising solutions for improving the platinum utilization and long-term stability of SAFCs by using the oxidized graphene multi-layer material as a separator and platinum substrate.

Conflicts of Interest: The authors declare no conflict of interest.

References

1. Boysen, D.A.; Uda, T.; Chisholm, C.R.I.; Haile, S.M. High-Performance Solid Acid Fuel Cells through Humidity Stabilization. *Science* **2004**, *303*, 68–70. [CrossRef] [PubMed]
2. Haile, S.M. Fuel cell materials and components. *Acta Mater.* **2003**, *51*, 5981–6000. [CrossRef]
3. Uda, T.; Haile, S.M. Thin-Membrane Solid-Acid Fuel Cell. *Electrochem. Solid-State Lett.* **2005**, *8*, A245. [CrossRef]
4. Haile, S.M.; Boysen, D.A.; Chisholm, C.R.I.; Merle, R.B. Solid acids as fuel cell electrolytes. *Nature* **2001**, *410*, 910–913. [CrossRef] [PubMed]
5. Ikeda, A.; Kitchaev, D.A.; Haile, S.M. Phase behavior and superprotonic conductivity in the $Cs_{1-x}Rb_xH_2PO_4$ and $Cs_{1-x}K_xH_2PO_4$ systems. *J. Mater. Chem. A* **2014**, *2*, 204–214. [CrossRef]
6. Sanghvi, S.; Haile, S.M. Experimental Crystal Structure Determination. *Solid State Ion.* **2020**, *349*, 15291.
7. Bagryantseva, I.N.; Ponomareva, V.G.; Khusnutdinov, V.R. Intermediate temperature proton electrolytes based on cesium dihydrogen phosphate and poly(vinylidene fluoride-co-hexafluoropropylene). *J. Mater. Sci.* **2021**, *56*, 14196–14206. [CrossRef]
8. Navarrete, L.; Andrio, A.; Escolástico, S.; Moya, S.; Compañ, V.; Serra, J.M. Protonic Conduction of Partially-Substituted CsH2PO4 and the Applicability in Electrochemical Devices. *Membranes* **2019**, *9*, 49. [CrossRef]
9. Hosseini, S.; Daud, W.R.W.; Badiei, M.; Mohammad, A.B. Effect of surfactants in synthesis of CsH_2PO_4 as protonic conductive membrane. *Bull. Mater. Sci.* **2011**, *34*, 759–765. [CrossRef]
10. Singh, D.; Kumar, P.; Singh, J.; Veer, D.; Kumar, A.; Katiyar, R.S. Structural, thermal and electrical properties of composites electrolytes $(1-x) CsH_2PO_4/x\ ZrO_2$ ($0 \leq x \leq 0.4$) for fuel cell with advanced electrode. *SN Appl. Sci.* **2021**, *3*, 46. [CrossRef]
11. Lu, X.; Yang, X.; Tariq, M.; Li, F.; Steimecke, M.; Li, J.; Varga, A.; Bron, M.; Abel, B. Plasma-etched functionalized graphene as a metal-free electrode catalyst in solid acid fuel cells. *J. Mater. Chem. A* **2020**, *8*, 2445–2452. [CrossRef]
12. Wagner, M.; Dreßler, C.; Lohmann-Richters, F.P.; Hanus, K.; Sebastiani, D.; Varga, A.; Abel, B. Mechanism of ion conductivity through polymer-stabilized CsH2PO4 nanoparticular layers from experiment and theory. *J. Mater. Chem. A* **2019**, *7*, 27367–27376. [CrossRef]
13. Lohmann-Richters, F.P.; Odenwald, C.; Kickelbick, G.; Abel, B.; Varga, A. Facile and scalable synthesis of sub-micrometer electrolyte particles for solid acid fuel cells. *RSC Adv.* **2018**, *8*, 21806–21815. [CrossRef]
14. Naumov, O.; Naumov, S.; Abel, B.; Varga, A. The stability limits of highly active nitrogen doped carbon ORR nano-catalysts: A mechanistic study of degradation reactions. *Nanoscale* **2018**, *14*, 6724–6733. [CrossRef]
15. Lohmann-Richters, F.P.; Abel, B.; Varga, A. In situ determination of the electrochemically active platinum surface area: Key to improvement of solid acid fuel cells. *J. Mater. Chem. A* **2018**, *6*, 2700–2707. [CrossRef]

16. Papandrew, A.B.; Chisholm, C.R.I.; Elgammal, R.A.; Ozer, M.M.; Zecevic, S.K. Advanced Electrodes for Solid Acid Fuel Cells by Platinum Deposition on CsH2PO4. *Chem. Mater.* **2011**, *23*, 1659–1667. [CrossRef]

17. Papandrew, A.B.; Chisholm, C.R.I.; Zecevic, S.K.; Veith, G.M.; Zawodzinski, T.A. Activity and Evolution of Vapor Deposited Pt-Pd Oxygen Reduction Catalysts for Solid Acid Fuel Cells. *J. Electrochem. Soc.* **2013**, *160*, F175. [CrossRef]

18. Lim, D.K.; Liu, J.; Pandey, S.A.; Paik, H.; Chisholm, C.R.I.; Hupp, J.T.; Haile, S.M. Atomic layer deposition of Pt@CsH$_2$PO$_4$ for the cathodes of solid acid fuel cells. *Electrochim. Acta* **2018**, *288*, 12–19. [CrossRef]

19. Daems, N.; Sheng, X.; Vankelecom, I.F.J.; Pescarmona, P.P. Metal-free doped carbon materials as electrocatalysts for the oxygen reduction reaction. *J. Mater. Chem. A* **2014**, *2*, 4085–4110. [CrossRef]

20. Samad, S.; Loh, K.S.; Wong, W.Y.; Lee, T.K.; Sunarso, J.; Chong, S.T.; Daud, W.R.W. Carbon and non-carbon support materials for platinum-based catalysts in fuel cells. *Int. J. Hydrog. Energy* **2018**, *43*, 7823–7854. [CrossRef]

21. Yin, S.; Mu, S.; Lv, H.; Cheng, N.; Pan, M.; Fu, Z. A highly stable catalyst for PEM fuel cell based on durable titanium diboride support and polymer stabilization. *Appl. Catal. B* **2010**, *93*, 233–240. [CrossRef]

22. He, P.; Liu, M.; Luo, J.L.; Sanger, A.R.; Chuang, K.T. Stabilization of Platinum Anode Catalyst in a H$_2$S-O$_2$ Solid Oxide Fuel Cell with an Intermediate TiO$_2$ Layer. *J. Electrochem. Soc.* **2002**, *149*, A808. [CrossRef]

23. Wagner, M.; Lorenz, O.; Lohmann-Richters, F.P.; Varga, A.; Abel, B. Study on solid electrolyte catalyst poisoning in solid acid fuel cells. *J. Mater. Chem. A* **2021**, *9*, 11347–11358. [CrossRef]

24. Prokop, M.; Drakselova, M.; Bouzek, K. Review of the experimental study and prediction of Pt-based catalyst degradation during PEM fuel cell operation. *Electrochim. Acta.* **2020**, *20*, 20–27. [CrossRef]

25. Beilstein, Z. Materials and characterization techniques for high-temperature polymer electrolyte membrane fuel cells. *J. Nanotechnol.* **2015**, *6*, 68–83.

26. Cho, E.; Yitamben, E.N.; Iski, E.V.; Guisinger, N.P.; Kuech, T.F. Atomic-Scale Investigation of Highly Stable Pt Clusters Synthesized on a Graphene Support for Catalytic Applications. *J. Phys. Chem. C* **2012**, *116*, 26066–26071. [CrossRef]

27. Tennyson, W.D.; Tian, M.; Papandrew, A.B.; Rouleau, C.M.; Puretzky, A.A.; Sneed, B.T.; More, K.L.; Veith, G.M.; Duscher, G.; Zawodzinski, T.A.; et al. Bottom up synthesis of boron-doped graphene for stable intermediate temperature fuel cell electrodes. *Carbon* **2017**, *123*, 605–615. [CrossRef]

28. Thoi, V.S.; Usiskin, R.E.; Haile, S.M. Platinum-decorated carbon nanotubes for hydrogen oxidation and proton reduction in solid acid electrochemical cells. *Chem. Sci.* **2015**, *6*, 1570–1577. [CrossRef] [PubMed]

29. Lee, H.B.R.; Bent, S.F. Formation of Continuous Pt Films on the Graphite Surface by Atomic Layer Deposition with Reactive O$_3$. *Chem. Mater.* **2015**, *27*, 6802–6809. [CrossRef]

30. Haile, S.M.; Chisholm, C.R.I.; Sasaki, K.; Boysen, D.A.; Uda, T. Solid acid proton conductors: From laboratory curiosities to fuel cell electrolytes. *Faraday Discuss.* **2007**, *134*, 17–39. [CrossRef]

31. Litster, S.; McLean, G. PEM fuel cell electrodes. *J. Power Sources* **2004**, *130*, 61–76. [CrossRef]

32. Sasaki, K.; Wang, J.X.; Balasubramanian, M.; McBreen, J.; Uribe, F.; Adzic, R.R. Ultra-low platinum content fuel cell anode electrocatalyst with a long-term performance stability. *Electrochim. Acta* **2004**, *49*, 3873–3877. [CrossRef]

33. Haug, A.T.; White, R.E.; Weidner, J.W.; Huang, W.; Shi, S.; Stoner, T.; Rana, N. Increasing Proton Exchange Membrane Fuel Cell Catalyst Effectiveness Through Sputter Deposition. *J. Electrochem. Soc.* **2002**, *149*, A280. [CrossRef]

34. Cha, S.Y.; Lee, W.M. Performance of Proton Exchange Membrane Fuel Cell Electrodes Prepared by Direct Deposition of Ultrathin Platinum on the Membrane Surface. *J. Electrochem. Soc.* **1999**, *146*, 4055. [CrossRef]

35. Wee, J.H.; Lee, K.Y.; Kim, S.H. Fabrication methods for low-Pt-loading electrocatalysts in proton exchange membrane fuel cell systems. *J. Power Sources* **2007**, *165*, 667–677. [CrossRef]

36. Singh, S.; Datta, J. Size control of Pt nanoparticles with stabilizing agent for better utilization of the catalyst in fuel cell reaction. *J. Mater. Sci.* **2010**, *45*, 3030–3040. [CrossRef]

37. Hsieh, C.; Liu, Y.; Tzou, D.; Chen, Y. Platinum electrocatalysts attached to carbon nanotubes by atomic layer deposition with different cycle numbers. *J. Taiwan Inst. Chem. Eng.* **2014**, *45*, 186–191. [CrossRef]

38. Liang, X.; Jiang, C. Atomic layer deposited highly dispersed platinum nanoparticles supported on non-functionalized multiwalled carbon nanotubes for the hydrogenation of xylose to xylitol. *J. Nanopart. Res.* **2013**, *15*, 1890. [CrossRef]

39. Wang, X.; Zhang, C.; Jin, B.; Liang, X.; Wang, Q.; Zhaoa, Z.; Li, Q. Pt–Carbon interaction-determined reaction pathway and selectivity for hydrogenation of 5-hydroxymethylfurfural over carbon supported Pt catalysts. *Catal. Sci. Technol.* **2021**, *11*, 1298–1310.

40. Hsieh, C.; Chen, W.; Tzou, D.; Roy, A.K.; Hsiao, H. Atomic layer deposition of Pt nanocatalysts on graphene oxide nanosheets for electro-oxidation of formic acid. *Int. J. Hydrog. Energy* **2012**, *37*, 17837–17843. [CrossRef]

41. Sun, S.; Zhang, G.; Gauquelin, N.; Chen, N.; Zhou, J.; Yang, S.; Chen, W.; Meng, X.; Geng, D.; Banis, M.N.; et al. Single-atom Catalysis Using Pt/Graphene Achieved through Atomic Layer Deposition. *Sci. Rep.* **2013**, *3*, 1775. [CrossRef]

42. Hu, Y.; Lu, J.; Feng, H. Surface modification and functionalization of powder materials by atomic layer deposition: A review. *RSC Adv.* **2021**, *11*, 11918–11942. [CrossRef]

43. Hsueh, Y.; Wang, C.; Kei, C.; Lin, Y.; Liu, C.; Perng, T. Fabrication of catalyst by atomic layer deposition for high specific power density proton exchange membrane fuel cells. *J. Catal.* **2012**, *294*, 63–68. [CrossRef]

44. Shu, T.; Liao, S.; Hsieh, C.; Roy, A.K.; Liu, Y.; Tzou, D.; Chen, W. Fabrication of platinum electrocatalysts on carbon nanotubes using atomic layer deposition for proton exchange membrane fuel cells. *Electrochim. Acta* **2012**, *75*, 101–107. [CrossRef]

45. Ritaka, M.; Leskelä, M. *Handbook of Thin Film Material*; Nalwa, H.S., Ed.; Academic Press: San Diego, CA, USA, 2001; Volume 1, p. 103.

46. Puurunen, R.L. Surface chemistry of atomic layer deposition: A case study for the trimethylaluminum/water process. *J. Appl. Phys.* **2005**, *97*, 121301. [CrossRef]

47. George, S.M. Atomic Layer Deposition: An Overview. *Chem. Rev.* **2010**, *110*, 111–131. [CrossRef]

48. Lee, W.; Bera, S.; Kim, C.M.; Koh, E.; Hong, W.; Oh, S.; Cho, E.; Kwon, S. Synthesis of highly dispersed Pt nanoparticles into carbon supports by fluidized bed reactor atomic layer deposition to boost PEMFC performance. *NPG Asia Mater.* **2020**, *12*, 40. [CrossRef]

49. Biró, L.P.; Lambin, P. Grain boundaries in graphene grown by chemical vapor deposition. *New J. Phys.* **2013**, *15*, 035024. [CrossRef]

50. Yazyev, O.V.; Chen, Y.P. Polycrystalline graphene and other two-dimensional materials. *Nat. Nanotechnol.* **2014**, *9*, 755–767. [CrossRef]

51. Shaina, P.R.; George, L.; Yadav, V.; Jaiswal, M. Estimating the thermal expansion coefficient of graphene: The role of graphene–substrate interactions. *J. Phys.: Condens. Matter* **2016**, *28*, 085301. [CrossRef]

52. Li, P.; Jing, G.; Zhang, B.; Sando, S.; Cui, T. Single-crystalline monolayer and multilayer graphene nano switches. *Appl. Phys. Lett.* **2014**, *104*, 113110. [CrossRef]

53. Sun, Z.; Raji, A.R.O.; Zhu, Y.; Xiang, C.; Yan, Z.; Kittrell, C.; Samuel, E.L.G.; Tour, J.M. Large-Area Bernal-Stacked Bi-, Tri-, and Tetralayer Graphene. *ACS Nano* **2012**, *6*, 9790–9796. [CrossRef] [PubMed]

54. Ferrari, A.C.; Meyer, J.C.; Scardaci, V.; Casiraghi, C.; Lazzeri, M.; Mauri, F.; Piscanec, S.; Jiang, D.; Novoselov, K.S.; Roth, S.; et al. Raman Spectrum of Graphene and Graphene Layers. *Phys. Rev. Lett.* **2006**, *97*, 187401. [CrossRef]

55. Lee, D.S.; Riedl, C.; Krauss, B.; von Klitzing, K.; Starke, U.; Smet, J.H. Raman spectra of epitaxial graphene on SiC and of epitaxial graphene transferred to SiO_2. *Nano Lett.* **2008**, *8*, 4320–4325. [CrossRef] [PubMed]

56. Marichy, C.; Pinna, N. Carbon-nanostructures coated/decorated by atomic layer deposition: Growth and applications. *Coord. Chem. Rev.* **2013**, *257*, 3232–3253. [CrossRef]

57. Bui, H.V.; Grillo, F.; Helmer, R.; Goulas, A.; van Ommen, J.R. Controlled Growth of Palladium Nanoparticles on Graphene Nanoplatelets via Scalable Atmospheric Pressure Atomic Layer Deposition. *J. Phys. Chem. C* **2016**, *120*, 8832–8840.

58. Xin, Y.; Liu, J.; Jie, X.; Liu, W.; Liu, F.; Yin, Y.; Gu, J.; Zoua, Z. Preparation and electrochemical characterization of nitrogen doped graphene by microwave as supporting materials for fuel cell catalysts. *Electrochim. Acta* **2012**, *60*, 354–358. [CrossRef]

59. Qi, Z.; Zhu, X.; Jin, H.; Zhang, T.; Kong, X.; Ruoff, R.S.; Qiao, Z.; Ji, H. Rapid Identification of the Layer Number of Large-Area Graphene on Copper. *Chem. Mater.* **2018**, *30*, 2067–2073. [CrossRef]

60. Yen, W.C.; Chen, Y.Z.; Yeh, C.H.; He, J.H.; Chiu, P.W.; Chueh, Y.L. Direct growth of self-crystallized graphene and graphite nanoballs with Ni vapor-assisted growth: From controllable growth to material characterization. *Sci. Rep.* **2014**, *4*, 4739. [CrossRef] [PubMed]

61. Aaltonen, T.; Ritala, M.; Sajavaara, T.; Keinonen, J.; Leskelä, M. Atomic Layer Deposition of Platinum Thin Films. *Chem. Mater.* **2003**, *15*, 1924–1928. [CrossRef]

62. Li, X.; Cai, W.; An, J.; Kim, S.; Nah, J.; Yang, D.; Piner, R.; Velamakanni, A.; Jung, I.; Tutuc, E.; et al. Large-Area Synthesis of High-Quality and Uniform Graphene Films on Copper Foils. *Science* **2009**, *324*, 1312–1314. [CrossRef] [PubMed]

63. Liao, L.; Duan, X. Graphene–dielectric integration for graphene transistors. *Mater. Sci. Eng. R* **2010**, *70*, 354–370. [CrossRef] [PubMed]

64. Lohmann, F.P.; Schulze, P.S.C.; Wagner, M.; Naumov, O.; Lotnyk, A.; Abel, B.; Varga, A. The next generation solid acid fuel cell electrodes: Stable, high performance with minimized catalyst loading. *J. Mater. Chem. A* **2017**, *5*, 15021–15025. [CrossRef]

65. Louie, M.W.; Haile, S.M. Platinum thin film anodes for solid acid fuel cells. *Energy Env. Sci.* **2011**, *4*, 4230–4238. [CrossRef]

66. Geim, A.K.; Novoselov, K.S. The rise of graphene. *Nat. Mater.* **2007**, *6*, 183–191. [CrossRef]

67. Lee, C.; Wei, X.; Kysar, J.W.; Hone, J. Measurement of the Elastic Properties and Intrinsic Strength of Monolayer Graphene. *Science* **2008**, *321*, 385–388. [CrossRef]

68. Mortazavi, B. Ultrahigh thermal conductivity and strength in direct-gap semiconducting graphene-like BC6N: A first-principles and classical investigation. *Carbon* **2021**, *182*, 373–383. [CrossRef]

69. Lee, W.; Lim, G.; Ko, S.H. Significant thermoelectric conversion efficiency enhancement of single layer graphene with substitutional silicon dopants. *Nano Energy* **2021**, *87*, 106188. [CrossRef]

70. Gong, S.; Jiang, L.; Cheng, Q. Robust bioinspired graphene-based nanocomposites via synergistic toughening of zinc ions and covalent bonding. *J. Mater. Chem. A* **2016**, *4*, 17073–17079. [CrossRef]

71. Li, W.; Chen, B.; Meng, C.; Fang, W.; Xiao, Y.; Li, X.Y.; Hu, Z.F.; Xu, Y.X.; Tong, L.; Wang, H.Q.; et al. Ultrafast All-Optical Graphene Modulator. *Nano Lett.* **2014**, *14*, 955–959. [CrossRef]

72. El Abbassi, M.; Sangtarash, S.; Liu, X.; Perrin, M.L.; Braun, O.; Lambert, C.; Jan van der Zant, H.S.; Yitzchaik, S.; Decurtins, S.; Liu, S.; et al. Robust graphene-based molecular devices. *Nat. Nanotechnol.* **2019**, *14*, 957–961. [CrossRef]

73. Singh, A.K.; Chaudhary, V.; Kumar, A.; Sinhaa, S.R.P. Investigation of electronic properties of chemical vapor deposition grown single layer graphene via doping of thin transparent conductive films. *RSC Adv.* **2021**, *11*, 3096. [CrossRef]

74. Bandosz, T.J.; Wang, S.; Minami, D.; Kaneko, K. Robust graphene-based monoliths of homogeneous ultramicroporosity. *Carbon* **2015**, *87*, 87–97. [CrossRef]

75. Nirmalraj, P.N.; Lutz, T.; Kumar, S.; Duesberg, G.S.; Boland, J.J. Nanoscale Mapping of Electrical Resistivity and Connectivity in Graphene Strips and Networks. *Nano Lett.* **2011**, *11*, 16–22. [CrossRef]

76. Novoselov, K.S.; Geim, A.K.; Morozov, S.V.; Jiang, D.; Katsnelson, M.I.; Grigorieva, I.M.; Dubonos, S.V.; Firsov, A.A. Two-dimensional gas of massless Dirac fermions in graphene. *Nature* **2005**, *438*, 197–200. [CrossRef]

77. Hwang, E.H.; Sarma, S.D. Acoustic phonon scattering limited carrier mobility in two-dimensional extrinsic graphene. *Phys. Rev. B.* **2008**, *77*, 115449. [CrossRef]

78. Berger, C.; Song, Z.; Li, X.; Wu, X.; Brown, N.; Naud, C.; Mayou, D.; Li, T.; Haas, J.; Marchenkov, A.N.; et al. Electronic Confinement and Coherence in Patterned Epitaxial Graphene. *Science* **2006**, *312*, 1191–1196. [CrossRef] [PubMed]

79. Tan, Y.; Zhang, Y.; Stormer, H.L.; Kim, P. Temperature dependent electron transport in graphene. *Eur. Phys. J. Spec. Top.* **2007**, *148*, 15–18. [CrossRef]

80. Bolotin, K.I.; Sikes, K.J.; Jiang, Z.; Klima, M.; Fudenberg, G.; Hone, J.; Kim, P.; Stormer, H.L. Ultrahigh electron mobility in suspended graphene. *Solid State Commun.* **2008**, *146*, 351–355. [CrossRef]

81. Bolotin, K.I.; Sikes, K.J.; Hone, J.; Stormer, H.L.; Kim, P. Temperature-Dependent Transport in Suspended Graphene. *Phys. Rev. Lett.* **2008**, *101*, 096802. [CrossRef]

82. Morozov, S.V.; Novoselov, K.S.; Katsnelson, M.I.; Schedin, F.; Elias, D.C.; Jaszczak, J.A.; Geim, A.K. Giant Intrinsic Carrier Mobilities in Graphene and Its Bilayer. *Phys. Rev. Lett.* **2008**, *100*, 016602. [CrossRef] [PubMed]

83. Zhang, H.; Yang, D.; Lau, A.; Ma, T.; Lin, H.; Jia, B. Hybridized Graphene for Supercapacitors: Beyond the Limitation of Pure Graphene. *Small* **2021**, *17*, 2007311. [CrossRef]

84. Fang, X.; Yu, X.; Zheng, H.; Jin, H.; Wang, L.; Cao, M.S. Temperature- and thickness-dependent electrical conductivity of few-layer graphene and graphene nanosheets. *Phys. Lett. A* **2015**, *379*, 2245–2251. [CrossRef]

85. Griffin, E.; Mogg, L.; Hao, G.; Kalon, G.; Bacaksiz, C.; Lopez-Polin, G.; Zhou, T.Y.; Guarochico, V.; Cai, J.; Neumann, C.; et al. Proton and Li-Ion Permeation through Graphene with Eight-Atom-Ring Defects. *Acs Nano* **2020**, *14*, 7280–7286. [CrossRef]

86. Zhang, B.; Cao, Y.; Jiang, S.; Li, Z.; He, G.; Wu, H. Enhanced proton conductivity of Nafion nanohybrid membrane incorporated with phosphonic acid functionalized graphene oxide at elevated temperature and low humidity. *J. Membr. Sci.* **2016**, *518*, 243–253. [CrossRef]

87. Hatakeyama, K.; Karim, M.R.; Ogata, C.; Tateishi, H.; Taniguchi, T.; Koinuma, M.; Hayami, S.; Matsumoto, Y. Optimization of proton conductivity in graphene oxide by filling sulfate ions. *Chem. Commun.* **2014**, *50*, 14527–14530. [CrossRef]

88. Hamidah, N.L.; Shintani, M.; Fauzi, A.S.A.; Putri, G.K.; Kitamura, S.; Hatakeyama, K.; Sasaki, M.; Quitain, A.T.; Kida, T. Graphene Oxide Membranes with Cerium-Enhanced Proton Conductivity for Water Vapor Electrolysis. *ACS Appl. Nano Mater.* **2020**, *3*, 4292–4304. [CrossRef]

89. Hu, S.; Lozada-Hidalgo, M.; Wang, F.C.; Mishchenko, A.; Schedin, F.; Nair, R.R.; Hill, E.W.; Boukhvalov, D.W.; Katsnelson, M.I.; Dryfe, R.A.W.; et al. Proton transport through one-atom-thick crystals. *Nature* **2014**, *516*, 227–230. [CrossRef] [PubMed]

90. Lozada-Hidalgo, M.; Hu, S.; Marshall, O.; Mishchenko, A.; Grigorenko, A.N.; Dryfe, R.A.W.; Radha, B.; Grigorieva, I.V.; Geim, A.K. Sieving hydrogen isotopes through two-dimensional crystals. *Science* **2016**, *351*, 68–70. [CrossRef]

91. Sun, P.Z.; Yang, Q.; Kuang, W.J.; Stebunov, Y.V.; Xiong, W.Q.; Yu, J.; Nair, R.R.; Katsnelson, M.I.; Yuan, S.J.; Grigorieva, I.V.; et al. Limits on gas impermeability of graphene. *Nature* **2020**, *579*, 229–232. [CrossRef]

92. Zhang, H.; Lee, G.; Gong, C.; Colombo, L.; Cho, K. Grain Boundary Effect on Electrical Transport Properties of Graphene. *J. Phys. Chem. C* **2014**, *118*, 2338–2343. [CrossRef]

93. Simonis, P.; Goffaux, C.; Thiry, P.A.; Biro, L.P.; Lambin, P.; Meunier, V. STM study of a grain boundary in graphite. *Surf. Sci.* **2002**, *511*, 319–322. [CrossRef]

94. Gao, W.; Wu, G.; Janicke, M.T.; Cullen, D.A.; Mukundan, R.; Baldwin, J.K.; Brosha, E.L.; Galande, C.; Ajayan, P.M.; More, K.L.; et al. Ozonated Graphene Oxide Film as a Proton-Exchange Membrane. *Angew. Chem. Int. Ed. Engl.* **2014**, *53*, 3588–3593. [CrossRef] [PubMed]

95. Ambrosi, A.; Pumera, M. The CVD graphene transfer procedure introduces metallic impurities which alter the graphene electrochemical properties. *Nanoscale* **2014**, *6*, 472–476. [CrossRef] [PubMed]

96. Lehnert, J.; Spemann, D.; Hatahet, M.H.; Mändl, S.; Mensing, M.; Finzel, A.; Varga, A.; Rauschenbach, B. Graphene on silicon dioxide via carbon ion implantation in copper with PMMA-free transfer. *Appl. Phys. Lett.* **2017**, *110*, 233114. [CrossRef]

97. Olesik, J.W.; Gray, P.J. Considerations for measurement of individual nanoparticles or microparticles by ICP-MS: Determination of the number of particles and the analyte mass in each particle. *J. Anal. At. Spectrom.* **2012**, *27*, 1143–1155. [CrossRef]

98. dos Anjos, S.L.; Alves, J.C.; Rocha Soares, S.A.; Araujo, R.G.O.; de Oliveira, O.M.C.; Queiroz, A.F.S.; Ferreira, S.L.C. Multivariate optimization of a procedure employing microwave-assisted digestion for the determination of nickel and vanadium in crude oil by ICP OES. *Talanta* **2018**, *178*, 842–846. [CrossRef]

99. Yoshii, K.; Yamaji, K.; Tsuda, T.; Matsumoto, H.; Sato, T.; Izumi, R.; Torimotoc, T.; Kuwabata, S. Highly durable Pt nanoparticle-supported carbon catalysts for the oxygen reduction reaction tailored by using an ionic liquid thin layer. *J. Mater. Chem. A* **2016**, *4*, 12152–12157. [CrossRef]